Differentiating Defects and Their Influence on Hematite Photoanodes Using X-ray Absorption Spectroscopy and Raman Microscopy

Yutong Liu[a], Rodney D. L. Smith[a,b,*]

[a]*Department of Chemistry, University of Waterloo, 200 University Avenue W., Waterloo, Ontario, Canada N2L 3G1*

[b]*Waterloo Institute for Nanotechnology, University of Waterloo, 200 University Avenue W., Waterloo, Ontario, Canada N2L 3G1*

Correspondence to:

rodsmith@uwaterloo.ca

ABSTRACT

A high degree of variability in behavior and performance of hematite as photoanodes for the oxygen evolution reaction signifies a need to improve our understanding of the interplay between defects and photoelectrochemical performance. We approach this problem by applying structure-property analysis to a series of hematite samples synthesized under either O_2 or N_2 environments such that they exhibit highly variable performance for photoelectrocatalytic oxygen evolution. X-ray absorption fine-structure spectroscopy and Raman spectroscopy provide parameters describing the structure of samples across the series. Systematic comparisons of these parameters to those describing photoelectrochemical performance reveal different defects in samples prepared under N_2 or O_2. Distinct correlations between both iron oxidation state and charge carrier density with photoelectrocatalytic performance lead to assignment of the primary defects as oxygen vacancies (N_2) and iron vacancies (O_2). Differences in the structural distortions caused by these defects are seen in correlations between short-range structural parameters and photoelectrochemical behavior. These distortions are readily observed by Raman spectroscopy, suggesting that it may be possible to calibrate the width, energy, and intensity of peaks in Raman spectra to enable direct analysis of defects in hematite photoanodes.

Keywords: photoelectrocatalysis, defect analysis, Raman spectroscopy, X-ray absorption spectroscopy, hematite, oxygen evolution reaction

INTRODUCTION

Photoelectrodes and photoelectrochemical (PEC) reactions are being developed with the intent of enabling efficient solar energy storage schemes.[1,2] Beyond such practical applications, PEC reactions also provide a wealth of opportunities to advance fundamental knowledge pertaining to the bonding and electronic structure of solids. Photon absorption by a photoanode is followed by an intricate network of competing elementary processes – the desired reaction proceeds only when the photoexcited electron does not follow paths such as recombination. The thermodynamic and kinetic properties of these elementary reactions can be altered by modifications to the bonding structure, electronic structure, or interfacial structure of a photoelectrode.[3–5] The presence of structural defects within solid-state photoanodes therefore has a direct impact on the observed PEC behavior. We are interested in using such changes in PEC behavior to develop simple methods for defect analysis in materials commonly used as photoelectrodes.

Photoanodes for the oxygen evolution reaction (OER) are arguably the most widely studied photoelectrodes for PEC reactions. They are critical in solar fuel schemes because they provide the electrons and protons required by the cathodic reactions such as hydrogen evolution, CO_2 reduction and N_2 reduction.[6–9] Numerous photoanode materials are studied for OER,[10] but hematite (α-Fe_2O_3) remains one of the most intensely studied options. Hematite offers an earth abundant composition, a near ideal band gap of 2.1 eV, and a theoretical maximum value 12.5 mA cm^{-2}.[11,12] Hematite also stands out because the maximum attained photocurrent density, the onset of photoelectrocatalysis, the shape of current-voltage response, and surface reaction kinetics all exhibit significant variation across the literature. These variations make it apparent that hematite samples synthesized in different labs are rarely identical; data that is conventionally reported, however, makes it impossible to determine the differences. It is known that hematite natively accommodates several types of defects,[13] including vacancies in iron[14,15] or oxygen sites,[16,17] interstitial iron ions,[18] and even interstitial protons.[19,20] Such defects are challenging to diagnose, and even more challenging to quantify. Techniques that facilitate the diagnosis and quantification of all possible defects would enable major advances in the field.

Point defects in hematite have been discussed across the literature, with substantial interest focused on oxygen vacancies. Being an *n*-type semiconductor, the charge carrier density (N_d) of hematite is influenced by the concentration of oxygen vacancies. These vacancies are native defects that can be altered by post-synthetic treatments. Treatment of hematite with an oxygen plasma, or by annealing at high temperature in oxygen rich or deficient atmospheres are two such treatments.[17,21] Increasing the concentration of oxygen defects has been shown to enhance PEC performance by increasing N_d.[21] More complex roles for these defects have also been noted: they may serve as recombination centers when located at the semiconductor-electrolyte interface,[22] narrow the depletion layer and boost the charge separation and transfer efficiencies,[23,24] or enhance the kinetics for water oxidation at the surface.[24,25] Atomistic modeling has explored possible migration pathways for oxygen vacancies in hematite.[26] Evidence suggests that oxygen vacancies can be accompanied by iron vacancies.[27] Iron vacancies themselves have been implicated as the main defect responsible for the activity of hematite as photoanodes.[14–16] They have, however, received much less attention than oxygen vacancies. This is likely due to a combination of challenges spanning synthetic control and experimental characterization. X-ray diffraction (XRD) measurements are capable of identifying magnetite formation upon introduction of excess oxygen vacancies, but the oxygen vacancies themselves cannot be confidently measured by XRD due to oxygen's weak scattering relative to iron.[22,28] Oxygen vacancies are frequently identified and quantified indirectly through measurement of charge carrier density, which necessitates the assumption that all charge carriers are derived from oxygen vacancies. Defects such as protohematite are similarly difficult to diagnose using XRD, with past diagnosis requiring high-resolution synchrotron measurements.[19,29] A full understanding of the defect structure of hematite photoanodes requires the ability to routinely deconvolute the effect of the various defects that can form. The exquisite sensitivity of Raman spectroscopy to lattice distortions is well documented,[30,31]but the information is indirect and requires comparison with direct structural information. X-ray absorption spectroscopy is uniquely capable of simultaneously providing information pertaining to both electronic and bonding structure, making it an ideal candidate for comparison with Raman spectra.

Herein, we combine X-ray absorption spectroscopy, Raman spectroscopy and photoelectrochemical measurements to demonstrate that fabrication conditions yield a transition in dominance between two unique defects in hematite electrodes. Structure-property

analysis across a series of hematite photoanodes prepared by annealing lepidocrocite shows that N_2 annealing environments favor oxygen vacancies, while O_2 annealing environments favor iron vacancies. The absolute and relative gains in current density at 1.23 V are greater for samples annealed under O_2 than those under N_2, suggesting that removal of iron vacancies is critical to enhancing PEC performance. We propose that peaks observed in Raman spectra can serve to identify defects in hematite.

EXPERIMENTAL

Hematite Fabrication. Lepidocrocite (γ-FeOOH) thin films were electrodeposited on fluorine-doped tin oxide coated aluminum borosilicate glass (FTO/ABS; Solaronix S.A.). FTO/ABS glass substrate pieces were cleaned by sequential ultrasonication in a detergent solution, milli-Q H_2O, then isopropanol. The surface was dried under a stream of N_2 and placed in a custom UV-irradiation chamber (GHO18T5VH lamp, Atlantic Ultraviolet) for 15 minutes. A solution containing 0.02 M ferrous chloride tetrahydrate (ACS reagent grade, Alfa Aesar) and 1M ammonium chloride (ACS reagent grade, EMD Chemicals Inc.) was purged with N_2 for 30 min before electrodeposition. A 0.1 M KOH (>85%, Sigma-Aldrich) solution was added to adjust solution pH to 7.0. Freshly cleaned FTO/ABS electrodes were held at 0.0 V *vs.* Ag/AgCl (sat'd KCl) for 7 min at room temperature with continuous N_2 purging. A series of 12 such electrodeposited γ-FeOOH films were converted to hematite by heating at 800 °C under varied conditions. These 12 conditions consisted of combinations of either N_2 or O_2 atmosphere with selected reaction times (0.2, 0.5, 1, 2, 4 and 8 h). Each photoanode was then cut into two pieces and rinsed with isopropanol. Each of the two halves was analyzed by Raman microscopy to ensure consistency (see below). One half of each sample was then used for photoelectrochemical measurement. The second half was used for analysis by X-ray absorption spectroscopy.

Raman Microscopy. Raman microscopic measurements were performed using a Renishaw inVia Reflex system. Raman microscopic mapping of each hematite film was performed using 1 μm steps across three different 4 μm x 4 μm grids. This approach was previously shown to offer consistent, representative spectra of each photoanode.[19] Spectra were acquired using a 100X objective, 633 nm excitation (Renishaw HeNe laser, 17 mW) filtered to 5% of maximum intensity, and an 1800 lines/mm diffraction grating. The Renishaw WiRE 5.3 software package

was used for spectrum processing, which included baseline subtraction, normalization, and curve fitting.

Photoelectrochemical Measurements. Photoanode properties and performance were measured using a Biologic SP-300 potentiostat and a Sciencetech A1 Lightline solar simulator equipped with an AM 1.5G filter. Hematite-coated FTO working electrodes were mounted as windows in a custom-made polyethylene cell. The cell contains a 1.54 cm^2 circular hole surrounded by a silicone O-ring. The hematite-coated FTO electrodes were clamped against the O-ring such that the cell could be operated using back-side illumination. Aqueous 1 M KOH electrolyte solutions were prepared using milliQ H_2O and KOH (>85%, Sigma-Aldrich). A Gaskatel HydroFlex Reversible Hydrogen Electrode (Gaskatel GmbH, Kassel, Germany) served as the reference electrode and a freshly cleaned piece of FTO as the counter electrode. The photoelectrochemical properties were measured by cyclic voltammetric sweeps, both in the dark and under illumination, from 0.4 to 1.7 V vs. RHE at 20 mV s^{-1}. Electrochemical impedance spectroscopy (EIS) was performed in the dark at 100 mV intervals between 0.5 to 1.3 V *vs*. RHE using a 10 mV amplitude.

X-ray Absorption Fine-Structure Spectroscopy. X-ray absorption spectroscopy (XAS) was performed at beamline 6-BM (BMM) at the National Synchrotron Light Source II (Brookhaven National Laboratory, NY, USA) using a Si(111) monochromator. The incident energy calibration was performed by beamline staff prior to the experiments. This was accomplished by determining the monochromator's angular position for the *K*-edge location of 10 transition metal elements. These values were then fitted to the Bragg equation using standardized values to obtain an angular offset and lattice constant for the monochromator. The Fe *K*-edge spectra were recorded between 6910 and 7960 eV in fluorescence mode for all 12 hematite samples. Data was acquired at intervals of 10 eV from 6910 to 7080 eV, 2 eV to 7100 eV, then 0.25 eV to 7135 eV. After this point the data was acquired with regular spacing of 0.05 A^{-1} in *k*-space. The detector was positioned 90 degrees relative to the incident beam. The samples were mounted on a motorized polycarbonate sample wheel. The wheel was positioned 45 degrees relative to the incident beam and rotated to change samples. Six spectra were acquired per sample using a four-element Si-drift detector. Real-time energy calibration was not possible due to the X-ray absorption of FTO-glass substrates. The experimental protocol was therefore designed to enable estimation of the temporal stability of the energy calibration and enable comparison of relative changes in XANES data. The six spectra for each sample

were split into two batches of pp three spectra, with measurements of each batch separated by approximately 24 hours. Comparison of the two batches of measurements show standard deviations of less than 0.04 eV in *K*-edge locations over the beamtime.

X-ray adsorption spectra were prepared for analysis by averaging all relevant spectra, subtraction of a linear baseline determined from the pre-edge region, and subsequent normalization of the post-edge region. The *K*-edge locations were defined as the point where the normalized data reached 0.5 units, using linear interpolation where necessary. The scattering amplitude, phase correction and mean free path for photoelectrons were calculated by *ab initio* calculations on a model crystalline hematite cluster using FEFF 8.4.[32] Structure models were then developed using the EXAFS equation with coordination number (N_i), bond length (R_i) and the mean standard deviation ($2\sigma_i^2$) for each relevant iron coordination shell. Errors in fitted parameters were estimated as previously described, using a useful *R*-space range of 1.5–4 Å.[33]

RESULTS & DISCUSSION

Sample Fabrication. A series 12 photoanodes with varied structural integrity were synthesized by systematic tuning of the conditions under which lepidocrocite precursor films were converted to hematite. Precursor films were anodically electrodeposited on FTO-coated glass substrates using a previously published approach.[34] These precursor films were heated at 800°C using combinations of six different annealing times (0.2, 0.5, 1, 2, 4 and 8 h) and two different gaseous environment (O_2 and N_2). Annealing of these films at temperatures above 550°C is known to induce a phase transition to hematite,[35,36] but previous results indicate that the consistent synthesis of hematite that is free of phase contaminations requires higher temperatures.[19,34,37] The synthesis of this photoanode series was strategically targeted to prepare the same nominal crystal structure with varied concentrations, and possibly identities, of structural defects. Each of these 12 photoanodes were comprehensively analyzed by X-ray absorption spectroscopy and Raman microscopy to obtain parameters describing their structure, and by photoelectrochemical experiments to obtain parameters describing their properties and behavior. The application of all techniques to each individual sample provides a robust sample-specific dataset that enables structure-property correlations to circumvent the sample-to-sample variability that is expected following wet-chemical syntheses such as that

employed here. High temperatures are known to affect the crystallinity and conductivity of FTO.[38,39] Uncompensated resistance values measured by EIS were between 10-30 Ω for most electrodes, but three increased to *ca*. 300 Ω and the sample annealed under N_2 for 8 hours uniquely yielded a cloudy glass substrate and measured uncompensated resistance values of 76 kΩ (Table S1). The sample prepared under N_2 for 8 h was therefore not used in correlational analysis.

X-ray Absorption Spectroscopy. X-ray absorption spectra confirm similarity in the overall structure for all but one of the hematite photoanodes, with subtle variations between the samples prepared under N_2 and O_2. The consistency of structure across 11 members of the sample series is visible in comparisons of their XAFS spectra (Figures 1A-1C). The consistency in these spectra enables an average to be calculated from them, with the sample heated under N_2 for 1 hour left out. The XANES region for this averaged data exhibits the characteristic structure for hematite,[40,41] with a minor pre-edge peak giving way to a strong white line with a distinct shoulder on the low energy side (Figure 1D). The associated EXAFS data contains strong oscillations that yield peaks rising above the noise level until *ca*. 8 Å in the Fourier transformed (FT) data (Figure 1E). The most prominent features in the FT data are three peaks, which lie near 1.6, 2.7 and 3.3 Å. The identities of these peaks are discussed in detail below. The XANES region for the sample heated under N_2 for 1 hour reveals a shift in *K*-edge location to lower energy, and a loss of the shoulder on the white line (Figure 1D). The EXAFS oscillations for this sample are clearly shifted relative to the other samples (Figure 1E); the FT data indicates substantial changes in bonding in the sample, with the shortest coordination shell shifting *ca*. 0.15 Å higher and the third shell shifting *ca*. 0.3 Å shorter. The sample annealed under N_2 for 1 hour is clearly contaminated with a second iron oxide phase. It is included in all subsequent analysis but is distinctively marked to indicate this contamination.

The Fe *K*-edge location for samples prepared under N_2 reside at lower energies than the overall average, while those synthesized under O_2 lie above the average. The *K*-edge locations (Figure 1F; Table S2) were determined by applying the half-height method to the fully processed, averaged spectrum for each sample.[42,43] The precision of each measurement is represented by the standard deviation across six individual scans that were acquired per sample. These values lie below 0.04 eV for all samples (Table S2). The six individual spectra for each sample were acquired in two batches of three, with measurements of each batch

separated by approximately 24 hours. The low variability between these batches (Figure S1), and the low overall standard deviation values, attest to the temporal stability of the energy calibration of the incident X-ray beam. The *K*-edge location is known to be linearly correlated to the oxidation state of the ions, with a shift of 4.6 eV per change in oxidation state expected for iron.[44,45] The *K*-edge values for samples annealed under O_2 lie between 7125.13 and 7125.17 eV, making them indistinguishable within the uncertainty of individual measurements (Figure 1F). Samples annealed under N_2 differ, showing a *K*-edge shift from 7125.13 eV to 7124.88 eV between 12 min and 4 h annealing times (with the 1h N_2 sample is left out). This range corresponds to a 0.06 unit change in the average oxidation state of iron ions in the films, or one in *ca*. 15 ions changing oxidation state. The 1 h N_2 sample exhibits an edge position of 7124.39 eV, which would suggest a 0.17 unit change if 1 h N_2 considered.

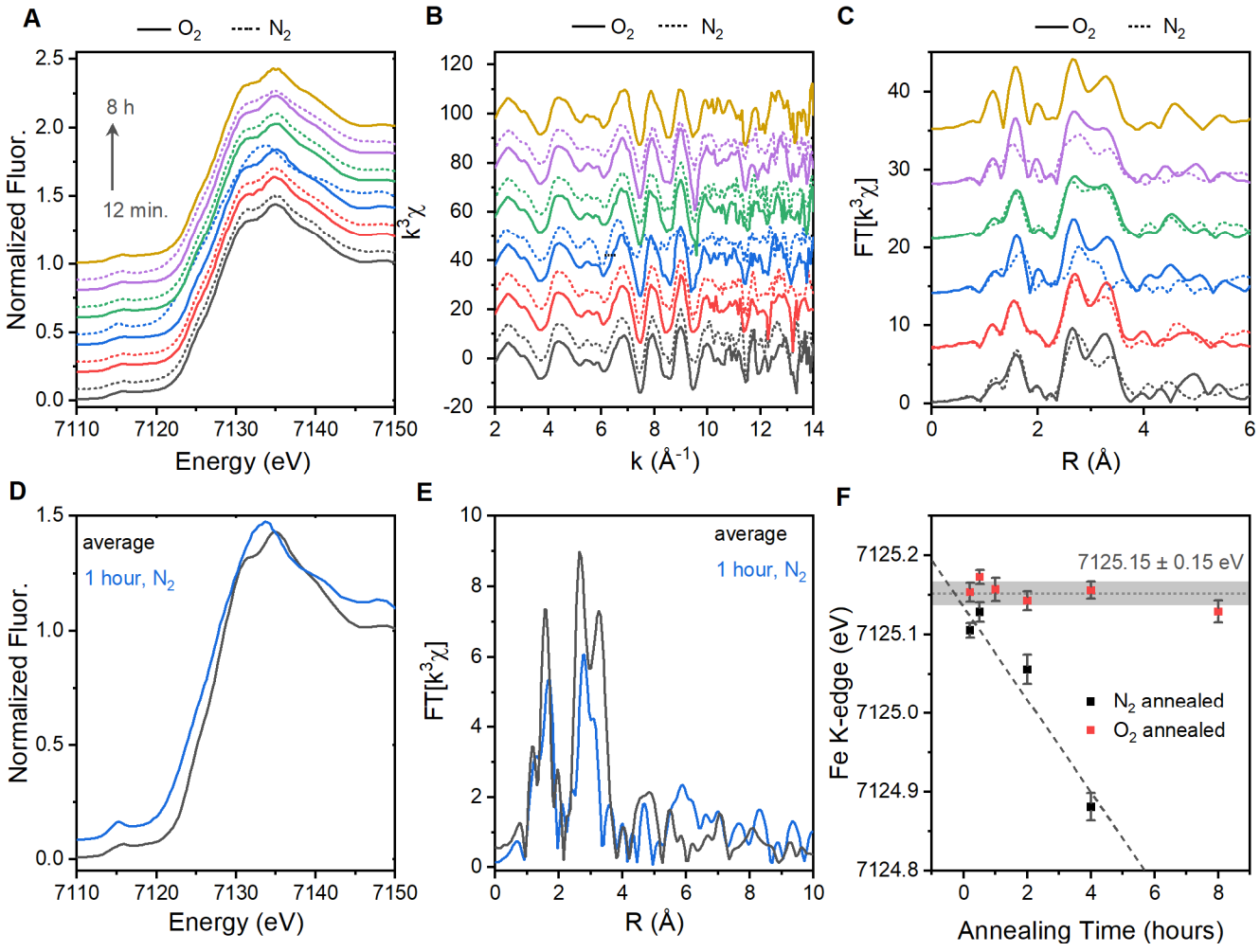

Figure 1. X-ray absorption fine-structure spectroscopy on hematite photoanode series. (A) Iron *K*-edge XANES, (B) EXAFS in *k*-space, and (C) Fourier transformed EXAFS spectra. Comparison of (D) XANES and (E) Fourier transformed EXAFS results for the 1 h N_2 sample

compared to the average of all other samples. (F) The iron *K*-edge location as a function of annealing time for the two environments, N_2 and O_2. Solid lines represent samples annealed under O_2 and dashed lines under N_2 in all panels. Annealing times follow the pattern highlighted in panel A.

Structural Model Development. A total of six coordination shells were selected for the development of structural models from EXAFS data, which exhibits major features between 1.5 and 3.8 Å (Figure 1C). The hematite crystal structure contains FeO_6 polyhedra arranged in a filled-filled-empty pattern along the crystal *c*-axis (Figure 2). Polyhedra are connected along this axis through face-sharing linkages, with each column linked to neighboring columns through edge-sharing and corner-sharing polyhedral motifs. This arrangement yields a single unique iron site with six coordination shells within 3.8 Å. Two unique Fe-O shells with coordination numbers of three exist, with 1.944 Å distances (labelled Fe-O_1) facing the empty interstitial sites and 2.116 Å distances (Fe-O_2) for the oxygen ions involved in face-sharing polyhedral motifs (Figure 2). The coordination shell for face sharing polyhedral Fe(III) ions has a coordination number of one and a distance of 2.898 Å (Fe-Fe_1), and edge sharing motifs have a coordination number of three and a distance of 2.969 Å (Fe-Fe_2). Two unique distances to corner-sharing iron ions in neighboring shells fall in this range, with a coordination number of three at 3.362 Å (Fe-Fe_3) and of six at 3.703 Å (Fe-Fe_4). All distances indicated above are from neutron diffraction data (ICSD #161283).[46]

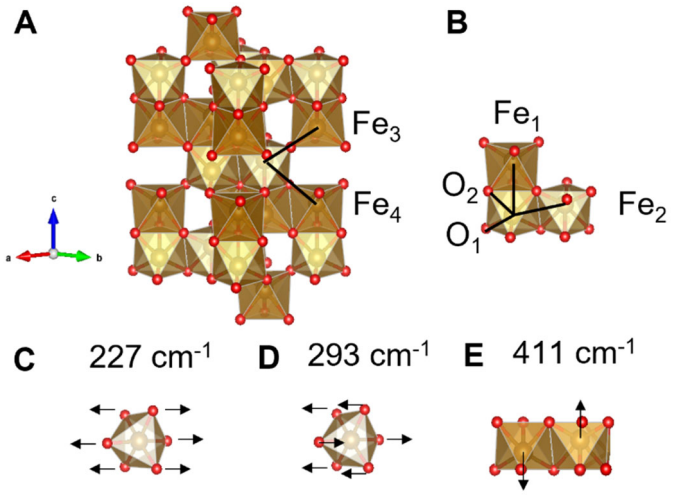

Figure 2. Structure of α-Fe_2O_3 and key features for analysis. (A) Unit cell of hematite with EXAFS distances Fe-Fe_3 and Fe-Fe_4 marked. (B) Face sharing and edge sharing motifs in hematite with EXAFS distances Fe-O_1, Fe-O_2, Fe-Fe_1 and Fe-Fe_2 marked. Raman vibrations used in structure-structure analysis at *ca*. (C) 227, (D) 293 and (E) 411 cm^{-1}. Graphics prepared using VESTA.[47]

Two different approaches were employed to develop models for quantitative analysis of the iron coordination environments using the six shells indicated above. To enable consideration of structural information that is not dependent on model development, the total intensity of each of the three observed peaks in the FT data was recorded for all samples (Table S2). The first simulation approach conservatively focused on fitting only $2\sigma_i^2$, the mean standard deviation values. This approach fixed all N_i at theoretical values and used fixed R_i values. Different R_i values were necessary for samples prepared under N_2 and O_2, with each set of values obtained by fitting an EXAFS spectrum of the average of all 6 samples in each respective dataset. The $2\sigma_i^2$ values were then fitted to provide an effective measure of relative disorder in each of the six coordination shells (Table S3). A second approach allowed both R_i and $2\sigma_i^2$ values to be fitted while maintaining theoretical N_i values. It was necessary to fix $2\sigma_{Fe\text{-}Fe1}^2$ during this approach due to overlap of features and a substantial defect-induced change in $R_{Fe\text{-}Fe1}$ noted in previous reports.[46] This second fitting process provides insight into structural expansion or contraction, along with relative disorder in each of the shells (Table S4).

Photoelectrochemical Properties. A series of three parameters describing photoelectrochemical (PEC) behavior were extracted to capture variations observed in the onset of photoelectrocatalytic oxygen evolution, the shape of the PEC curves and the maximum current densities attained. The photocurrent density at 1.23 V *vs*. RHE ($j_{1.23V}$) is a commonly reported performance parameter for OER on photoanodes that broadly captures photophysical and electrocatalytic properties (Figure 3A). The photocurrent density at 1.5 V *vs*. RHE ($j_{1.5V}$) was selected to capture the plateau in photocurrent density for each sample. The onset potential of photoelectrocatatlyic OER (E_{pec}) is a third term that showed clear trends with structural variation in a previous analysis. This value was calculated using a second derivative approach that was previously discussed.[19] Values for each of these three parameters are compiled in Table S5.

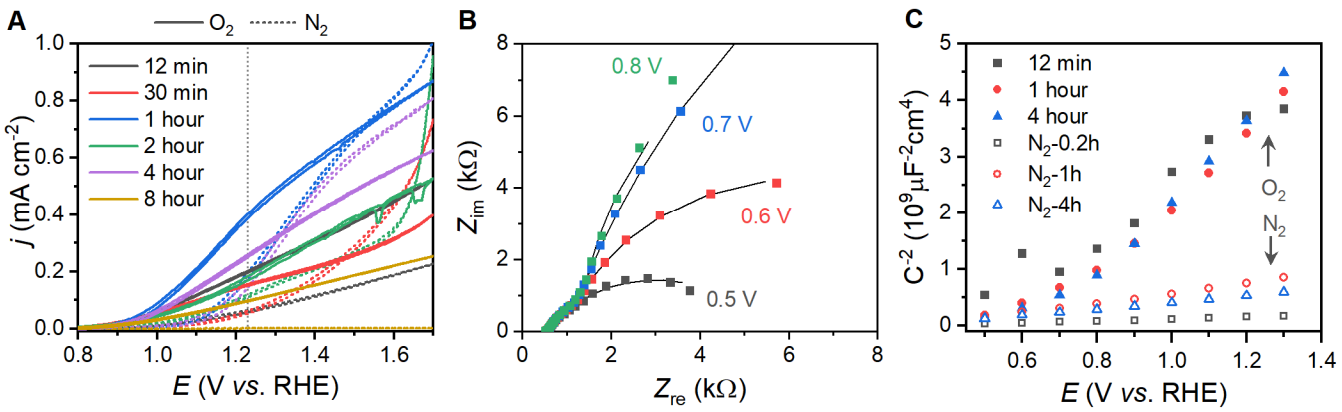

Figure 3. Photoelectrochemical behavior and electrochemical impedance spectroscopy results. (A) Voltammetric behavior under illumination for films annealed under different environments. (B) Nyquist plots of film annealed in N_2 for 12 min at select voltages to show influence of voltage. (C) Mott–Schottky plots of films prepared by annealing in different conditions. Solid lines represent samples annealed under O_2 and dashed lines under N_2.

Band-structure properties were measured using Mott-Schottky analysis. Potential-dependent EIS spectra acquired on samples in the dark contain a semicircle in Nyquist representations that changes radius with applied potential (Figure 3B). Simulations of the data using solution resistance (R_s) in series with parallel charge transfer resistance (R_{CT}) and space-charge capacitance (C_{SC}) circuit components enable measurement of these metrics for all samples (Table S5). Flat band potentials (E_{fb}) and charge carrier concentrations (N_d) for all samples were determined through Mott-Schottky analysis on the C_{SC} values (Figure 3C; Table S5).

Raman Spectroscopy. High quality Raman spectra were acquired for each of the photoanodes through a microscopic mapping protocol. The final spectra were acquired by averaging a total of 75 spectra per sample, with three sets of 25 spectra acquired in evenly spaced grids at three different 4 × 4 μm areas on the electrode surface. All 75 spectra are plotted for the sample annealed under O_2 for 4 hours to show the consistency of the spectra (Figure 4A). This approach was shown to yield consistent results that are representative of the overall film, where individual spectra showed a Gaussian distribution of peak intensity ratios with >85% of the spectra lying within 15% of the Gaussian maximum.[19] The data acquired here was at least as precise: the I_{293}/I_{411} ratio similarly captured >85% of spectra within 15% of the maxima, but the I_{411}/I_{612} yielded much sharper distribution with >85% of spectra within 3% of the maximum (Figure 4B). The averaged spectra all contain the seven characteristic Raman vibrations of hematite (Figure 4C), with four oxygen-based vibrations at 227, 246, 293, and 300

cm^{-1}, and three iron-based vibrations at 411, 496, and 612 cm^{-1}. In addition, a symmetry-forbidden E_u vibration appears at 660 cm^{-1}. The distortion-driven lowering of symmetry responsible for this feature has been discussed in the literature,[20,48,49] and the intensity of the Raman peak was critical in previous identification of defects in hematite.[19] This previous analysis showed annealing lepidocrocite films at 800°C yielded a decrease in intensity of the E_u vibration. Leaching of Sn(IV) from the FTO substrate was ruled out by this decrease in intensity, based on previous reports of extrinsic quadrivalent dopants increasing this E_u vibration by an order of magnitude.[50] In agreement with the XAS analysis, the sample annealed under N_2 for 1 hour shows unique differences that suggest phase impurity. The peaks at 246, 300, 411 and 612 cm^{-1} are substantially decreased in intensity, or completely missing. This sample provides a useful demonstration of the effect of phase impurities, but is excluded from correlational analysis. The location, width, and intensity of peaks are influenced by the structural integrity of the hematite photoanodes. Curve fitting of the spectra was performed to determine these three parameters (Table S6-S8).

Correlational Analysis. Systematic comparisons of the structural and the behavioral parameters identify relationships in the photoanode series. Samples were clustered into groups of photoanodes that were synthesized under O_2 and N_2. Each parameter in the dataset was then iteratively compared to all others in the dataset. The PEC behavior parameters (N_d, E_{fb}, $j_{1.23V}$, $j_{1.5V}$ and E_{PEC}), the XAFS parameters (Fe *K*-edge location FT peak intensities, $2\sigma_i^2$, and R_i) and the widths and locations of Raman peaks were used as is. The intensities of Raman vibrations are dependent on experimental parameters such that absolute intensities can be misleading; these values were therefore taken as the peak intensity ratio for all possible combinations of two peaks. Linear regression analysis was performed for each comparison and the resultant R^2 values were tabulated. Analysis of the results revealed correlations between structure and behavior (structure-property correlations) and between various structural parameters (structure-structure correlations). Relationship across the two data clusters, discussed below, lead us to conclude that oxygen vacancies are the dominant form of defect when the synthesis is performed under N_2, while iron vacancies become dominant under O_2.

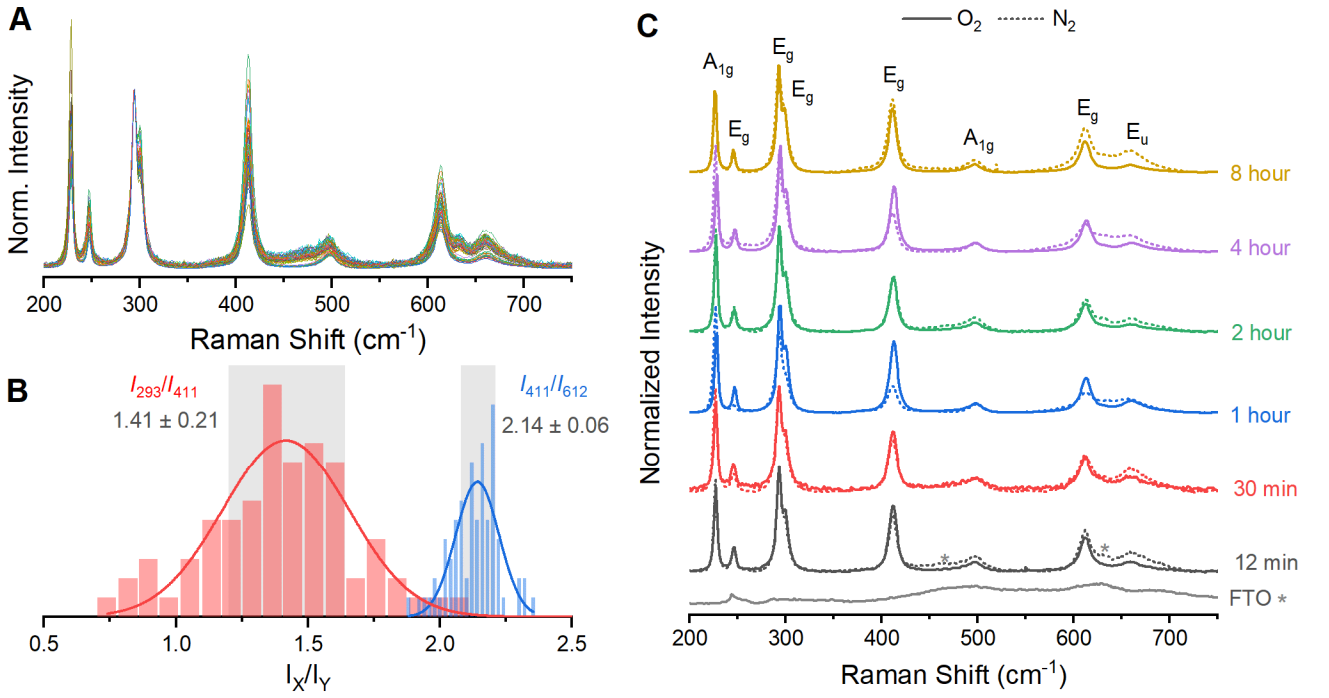

Figure 4. Raman spectra for hematite sample series. (A) All 75 spectra acquired over three 4×4 μm grids on the α-Fe_2O_3 sample annealed under O_2 for 4 hours and (B) a histogram showing the distribution of selected peak ratios. Solid line shows a Gaussian distribution fit of each histogram. Vertical shading denoting 85% of all spectra, captured by the ranges noted. (C) Spectra acquired by averaging all 75 individual spectra for each sample. Solid lines represent samples annealed under O_2 and dashed lines under N_2. Annealing times are marked along pairs of data.

Structure-Property Correlations. Distinct relationships are observed between the iron *K*-edge location and $j_{1.23V}$ for sample clusters prepared under N_2 and O_2. The $j_{1.23V}$ value for the O_2 cluster increases from 0.09 to 0.40 mA cm^{-2} while the *K*-edge location remains within the ca. 0.04 eV standard deviation values for individual edge measurements (Figure 5A). The N_2 cluster is markedly different, with *K*-edge values decreasing by 0.29 eV while $j_{1.23V}$ increases from 0.06 to 0.17 mA cm^{-2} (Figure 5A). The $j_{1.23V}$ values show signs of reaching a limiting plateau, a feature that is likely related to a tendency for hematite to transition to magnetite as Fe(II) accumulates.[22,51,52] The *K*-edge location of transition metal oxides are known to exhibit a linear correlation with the element's average oxidation state for small changes, with calibration curves from crystalline iron oxide standards estimating a shift of 4.6 eV per oxidation state for iron.[44,45] The 0.31 mA cm^{-2} increase observed in performance across the O_2 cluster thus occurs without a measurable change in iron oxidation state, while the average oxidation state of iron decreases by *ca*. 0.06 units for the 0.11 mA cm^{-2} increase in $j_{1.23V}$ for the N_2 cluster.

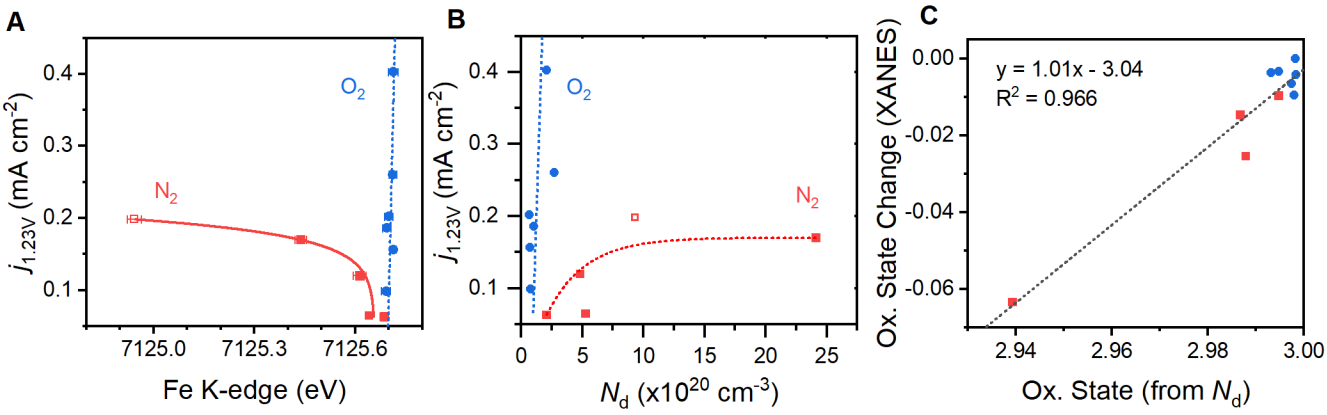

Figure 5. Correlations observed between XANES data and PEC properties across the sample series. (A) Correlation between Fe K-edge location and $j_{1.23V}$, and (B) between charge carrier density N_d and $j_{1.23V}$ across the entire series. (C) Comparison of change in oxidation states calculated by XANES with the oxidation state calculated from N_d. Error bars represent the standard deviation across six individual spectra for each sample.

The measured charge carrier densities exhibit a linear correlation to iron K-edge locations (Figure S2), providing a secondary measure that supports the trends seen in the XANES data. Electrons are the majority charge carrier in hematite, generated by native defects reducing the average iron oxidation state.[53] The O_2 cluster of samples exhibits a negligible change in N_d as $j_{1.23V}$ increases (Figure 5B). The N_2 cluster instead shows a 12-fold increase in N_d from 2.08 x 10^{20} to 2.41 x 10^{21} cm^{-3} as $j_{1.23V}$ increases. The paired observations of increasing charge carrier density and negative shift in the XANES K-edge location confirm that Fe(II) is associated with performance metrics across the N_2-annealed series, consistent with the formation of oxygen vacancies.[22,54] The absence of such changes in the O_2-annealed series provides evidence that a defect that is not associated with Fe(II) within the lattice controls photoelectrocatalytic performance. Crystallographic analysis of hematite shows a unit cell volume of 302 Å^3,[40,49] yielding an iron ion concentration of 3.97 x 10^{22} cm^{-3}. Assuming that charge carriers represent one electron per iron center (i.e., one Fe(III) converts to one Fe(II)), the ratio of N_d to total iron ion concentration yields the proportion of Fe(II) in each sample. Subtracting this ratio from 3 thus yields an estimate of the average oxidation state for iron ions. The relative oxidation state change across the series can be obtained from the XANES data by dividing the edge shift relative to a reference point, selected here to be the highest energy *K*-edge measured, by the expected shift of 4.6 eV per oxidation state.[44,45] The average oxidation

state calculated through these two techniques show excellent linear correlation (Figure 5C), with a slope of unity and an intercept on the XANES-derived axis of -3.04 – both of which are exactly what is predicted. The sample annealed under O_2 thus yield a stable average oxidation state for iron ions near 3, while the samples annealed under N_2 experience a decrease in oxidation state by up to 0.06 units.

Trends involving EXAFS structural parameters show that the unique changes in $j_{1.23V}$ for the two sample clusters are associated with distinct distortions of the average structure. The O_2 cluster of samples is primarily characterized by an increase in $j_{1.23V}$ as the distance across face-sharing iron ions ($R_{Fe\text{-}Fe1}$) increases from 2.854 to 2.900 Å (Figure 6A); the Fe-O shells remain essentially constant (Table S4). The N_2 cluster of samples instead show a *ca*. 0.060 Å contraction in $R_{Fe\text{-}O2}$ with increasing $j_{1.23V}$ (Figure 6A). An overall increase in structural disorder the N_2 cluster of samples is captured by a decrease in intensity of FT peaks with increasing $j_{1.23V}$ (Tables S2 and S5). The increase in disorder is captured in structural models as an increase in $2\sigma^2$ for all shells as $j_{1.23V}$ increases (Table S3). The structural distortion within the O_2 cluster of samples is therefore limited to iron-iron linkages, while the N_2 cluster experiences an overall contraction of Fe-O distances that disrupts all Fe-Fe distances in a seemingly non-systematic fashion.

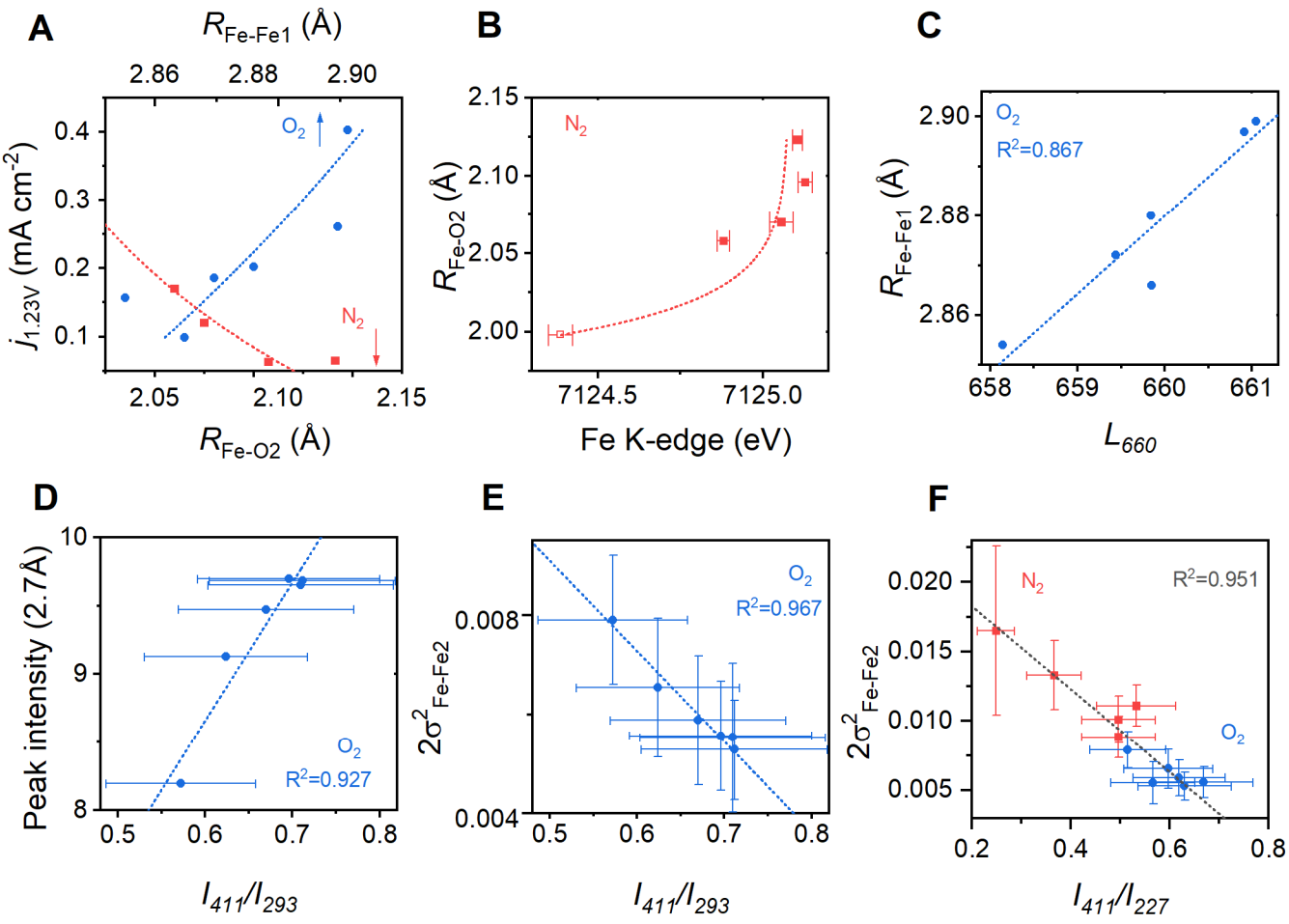

Figure 6. Correlations involving XAS derived parameters for hematite films annealed in N_2 and O_2. (A) Trends in photocurrent density $j_{1.23V}$ and Fe-Fe distance across face-sharing iron polyhedra (R_{Fe-Fe1}) for samples annealed under O_2, and Fe-O_2 distances for those annealed under N_2. (B) Iron-oxygen bond length increases with Fe K-edge values for samples annealed in N_2. (C) Location of the E_u vibration in Raman spectra as a function of R_{Fe-Fe1} for samples annealed in O_2. (D) Intensity of FT-EXAFS peak near 2.7 Å against the Raman intensity ratio I_{411}/I_{293} for hematite annealed in O_2. Correlation between mean standard relative deviation ($2\sigma^2_{Fe-Fe2}$) with Raman intensity ratios of (E) I_{411}/I_{293} for O_2 samples, and (F) $I_{411}I_{227}$ for hematite annealed in N_2 and O_2 environment.

The structural and behavioral parameters obtained for photoanodes prepared by annealing lepidocrocite films under N_2 provide clear evidence for oxygen vacancies being the dominant structural defect. Oxide vacancies are native defects in hematite that are accompanied by reduction of Fe(III) to Fe(II) within the lattice.[52] Thermal treatment of hematite under oxygen

deficient environments has been reported to improve photoelectrocatalytic performance by increasing N_d by altering the equilibria involving oxygen vacancy formation.[21] The observed correlations here are well aligned with these reports: the photoelectrocatalytic parameter $j_{1.23V}$ increases as the average oxidation state of iron decreases (Figure 5A), and as N_d increases (Figure 5B). Structure-property correlations suggest that $R_{Fe\text{-}O2}$ decreases as $j_{1.23V}$ increases, implying that oxide vacancies decrease Fe-O bond lengths (Figure 6A). Direct comparisons of oxide vacancy concentration and Fe-O bond lengths for hematite could not be found in the literature. The oxide vacancy-induced decrease in the radius of iron ions observed is nonetheless consistent with established trends in ionic radii, where ionic radius decreases as coordination numbers decrease.[55] Further, a correlation between the location of the iron *K*-edge and the Fe-O bond distances measured by EXAFS (Figure 6B) provides direct experimental support. Oxide vacancies are therefore the dominant defect present in hematite films prepared by thermal conversion of lepidocrocite under N_2 environments. These vacancies boost photoelectrocatalytic performance by increasing N_d, as previously reported.

The observed structural features and their correlations for photoanodes prepared by annealing lepidocrocite under O_2 are consistent with protohematite, α-$Fe_{2-x/3}O_{3-x}(OH)_x$,[56,57] being the dominant structural defect. This structure involves the trapping of positively charged protons within the crystal lattice, which is charge balanced by the formation of Fe(III) vacancies. This defect explains the stability of both measured N_d values and XANES K-edge locations across the O_2-annealed series. Previous variable-temperature synchrotron X-ray diffraction analysis showed that the trapping of protons and associated iron vacancies in protohematite induces overall compression relative to the hematite unit cell, distorting bonding (Table 1).[56,57] The largest magnitude change in bonding in that XRD analysis was a compression of face-sharing motifs ($R_{Fe\text{-}Fe1}$), with smaller expansion of corner-sharing motifs ($R_{Fe\text{-}Fe3}$). The Fe-O shells, in contrast, showed very little change. Structure-property analysis here shows that $j_{1.23V}$ values decrease with compression of $R_{Fe\text{-}Fe1}$ (Figure 6A), while $R_{Fe\text{-}O1}$ and $R_{Fe\text{-}O2}$ remain static (Table S4). The 660 cm^{-1} Raman peak is known to be an E_u lattice vibration that is formally symmetry forbidden but emerges following lattice distortions;[20,42] it has been proposed that protohematite induces such distortions.[19] The relationship between the E_u vibration, which is a shearing motion of Fe ions across face-sharing motifs, is further strengthened here by observation a 3 cm^{-1} red shift as $R_{Fe\text{-}Fe1}$ is compressed (Figure 6C). The results here are therefore consistent with the presence of varied concentrations of interstitial protons and associated iron vacancies

being the dominant structural defect for the O_2 cluster. These defects induce structural distortions, readily seen in Table 1 and Figure 6, that will alter bonding interactions within the material to affect semiconductor properties. Improvements to photoelectrocatalytic OER across the O_2 series are attributed to the removal of these lattice distortions, which yield performance gains that surpass those obtained for annealing under N_2 environment.

Table 1. Structural parameters of hematite and protohematite.

	Proto$_{313}$ [a]	**Proto$_{517}$** [a]	**Proto$_{779}$** [a]	**Hematite** [b]
$R_{Fe\text{-}O1}$	1.925	1.908	1.929	1.944
$R_{Fe\text{-}O2}$	2.122	2.158	2.137	2.116
$R_{Fe\text{-}Fe1}$	2.823	2.843	2.882	2.898
$R_{Fe\text{-}Fe2}$	2.945	2.955	2.971	2.969
$R_{Fe\text{-}Fe3}$	3.378	3.376	3.367	3.362
$R_{Fe\text{-}Fe4}$	3.686	3.688	3.702	3.703

[a] values from reference [56]
[b] values from neutron diffraction experiments in reference [46]

Additional correlations observed between features in the Raman spectra and structural parameters derived from EXAFS models may provide value in guiding synthetic efforts. Underlying the decrease in magnitude of Fe-Fe peaks in the EXAFS results (Figure 6D) is an increase in disorder in the Fe crystallographic sites. This disorder is captured by the mean standard relative displacement factor ($2\sigma^2$) in EXAFS models. The Fe-Fe$_2$ coordination shell yields the strongest peak in the FT EXAFS data (Figure 1), making it the most reliable to analyze. The above discussion on the defect-induced compression of the crystalline c-axis suggests that the 411 cm^{-1} should be important because it is the only Raman active vibration that involves movement of cations along the crystalline c-axis.[58,59] The $2\sigma^2_{Fe\text{-}Fe2}$ values do indeed yield strong negative correlations to the intensity of the 411 cm^{-1} peak relative to those at 293 (Figure 6E) and 227 cm^{-1} (Figure 6F), which involve synchronous movement of oxygen ions in the O1 and O2 sites. The observation of different structure-structure and structure-property correlations for the two clusters of samples provides evidence that each defect type has a unique influence on individual Raman vibrations, indicating that successful observation of correlations was reliant upon the ability to synthesize two series of samples where changes

in the concentration of a single defect dominated the observed changes in behavior. Variable temperature Raman spectroscopic analysis of phase transitions that occur when synthesizing hematite by annealing lepidocrocite suggest that protohematite forms between *ca*. 200 and 400°C.[29] The performance gains attained by removal of protohematite marks an understanding of their formation in, and elimination from, photoanodes as an important target for the community. This approach may enable deconvolution, and potentially the quantification, of all defects within a photoelectrode sample using only Raman spectroscopy. A substantial amount of work is clearly necessary to realize this capability, but systematic correlation of Raman spectra to structural information will yield a powerful tool for optimization of fabrication protocols and quality control.

CONCLUSIONS

Parameters describing the structure and photoelectrochemical properties of a series of hematite photoanodes were compared to each other to identify the prevalence of individual defects as a function of synthetic conditions. A series of 12 samples was synthesized by annealing lepidocrocite for varied times under either N_2 or O_2 environments. The interatomic distances and extent of disorder for short-range coordination shells was measured for each using X-ray absorption fine-structure spectroscopy, and the integrity of longer-range order was measured through Raman microscopy. Correlations between these structural descriptors with performance descriptors for photoelectrocatalytic oxygen evolution reaction leads us to conclude that the behavior of samples synthesized under N_2 is dictated by oxygen vacancies, while that for samples synthesized under O_2 is dictated by iron vacancies. Performance gains were achieved by either the removal of iron vacancies (O_2) or the introduction of oxygen vacancies (N_2). Comparison of the X-ray absorption results with Raman spectra reveals correlations that suggest it may be possible to calibrate the width, energy and intensity of peaks in Raman spectra to enable directly analysis of defects in hematite photoanodes.

CONFLICTS OF INTEREST

There are no conflicts to declare.

ACKNOWLEDGEMENTS

We thank the Natural Sciences and Engineering Research Council (NSERC) for support of this project through the Discovery Grants program. This document was prepared by University of Waterloo as a result of the use of facilities of the U.S. Department of Energy (DOE), which are managed by Brookhaven Science Associates, LLC, acting under Contract No. DE-SC0012704. Neither Brookhaven Science Associates, LLC,, DOE, the U.S. Government, nor any person acting on their behalf: (a) make any warranty or representation, express or implied, with respect to the information contained in this document; or (b) assume any liabilities with respect to the use of, or damages resulting from the use of any information contained in the document.

ASSOCIATED CONTENT

Electronic supplementary information is available. Tabulated parameters for XANES, two EXAFS, photoelectrochemical properties, and the intensity, width and location of individual Raman peaks. Comparison of the edge positions for individua XANES spectra. Correlation between charge carrier density and *K*-edge locations. Correlations between the intensity of FT-EXAFS peaks and photocurrent density for samples annealed in N_2.

REFERENCES

(1) Jiang, C.; Moniz, S. J. A.; Wang, A.; Zhang, T.; Tang, J. Photoelectrochemical Devices for Solar Water Splitting-Materials and Challenges. *Chem. Soc. Rev.* **2017**, *46*, 4645–4660.

(2) Park, K.; Kim, Y. J.; Yoon, T.; David, S.; Song, Y. M. A Methodological Review on Material Growth and Synthesis of Solar-Driven Water Splitting Photoelectrochemical Cells. *RSC Adv.* **2019**, *9*, 30112–30124.

(3) He, Y.; Hamann, T.; Wang, D. Thin Film Photoelectrodes for Solar Water Splitting. *Chem. Soc. Rev.* **2019**, *48*, 2182–2215.

(4) Piyadasa, A.; Wang, S.; Gao, P. X. Band Structure Engineering Strategies of Metal Oxide Semiconductor Nanowires and Related Nanostructures: A Review. *Semicond. Sci. Technol.* **2017**, *32*, 073001.

(5) Wang, S.; Liu, G.; Wang, L. Crystal Facet Engineering of Photoelectrodes for Photoelectrochemical Water Splitting. *Chem. Rev.* **2019**, *119*, 5192–5247.

(6) Govind Rajan, A.; Martirez, J. M. P.; Carter, E. A. Why Do We Use the Materials and Operating Conditions We Use for Heterogeneous (Photo)Electrochemical Water Splitting? *ACS Catal.* **2020**, *10*, 11177–11234.

(7) Xu, X. T.; Pan, L.; Zhang, X.; Wang, L.; Zou, J. J. Rational Design and Construction of Cocatalysts for Semiconductor-Based Photo-Electrochemical Oxygen Evolution: A Comprehensive Review. *Adv. Sci.* **2019**, *6*, 1801505.

(8) Strange, L. E.; Yadav, J.; Li, X.; Pan, S. Creating Electrocatalytic Heterojunctions for Efficient Photoelectrochemical CO_2 Reduction to Chemical Fuels. *J. Electrochem. Soc.* **2020**, *167*, 146518.

(9) Yan, Z.; Ji, M.; Xia, J.; Zhu, H. Recent Advanced Materials for Electrochemical and Photoelectrochemical Synthesis of Ammonia from Dinitrogen: One Step Closer to a Sustainable Energy Future. *Adv. Energy Mater.* **2020**, *10*, 1902020.

(10) Zhang, J.; Cui, J.; Eslava, S. Oxygen Evolution Catalysts at Transition Metal Oxide Photoanodes : Their Differing Roles for Solar Water Splitting. *Adv. Energy Mater.* **2021**, *11*, 2003111.

(11) Tamirat, A. G.; Rick, J.; Dubale, A. A.; Su, W. N.; Hwang, B. J. Using Hematite for Photoelectrochemical Water Splitting: A Review of Current Progress and Challenges. *Nanoscale Horizons*, **2016**, *1*, 243–267.

(12) Sivula, K.; Le Formal, F.; Grätzel, M. Solar Water Splitting: Progress Using Hematite (α-Fe_2O_3) Photoelectrodes. *ChemSusChem* **2011**, *4*, 432–449.

(13) Zhang, J.; Eslava, S. Understanding Charge Transfer, Defects and Surface States at Hematite Photoanodes. *Sustain. Energy Fuels* **2019**, *3*, 1351–1364.

(14) Negreiros, F. R.; Pedroza, L. S.; Souza, F. L.; Dalpian, G. M. Surface Fe Vacancy Defects on Haematite and Their Role in Light-Induced Water Splitting in Artificial Photosynthesis. *Phys. Chem. Chem. Phys.* **2017**, *19*, 31410–31417.

(15) Kraushofer, F.; Jakub, Z.; Bichler, M.; Hulva, J.; Drmota, P.; Weinold, M.; Schmid, M.; Setvin, M.; Diebold, U.; Blaha, P.; Parkinson, G. S. Atomic-Scale Structure of the Hematite α-Fe_2O_3(1102) “R-Cut” Surface. *J. Phys. Chem. C* **2018**, *122*, 1657–1669.

(16) Da Silva Alvim, R.; Ribeiro, F. N.; Dalpian, G. M. Iron and Oxygen Vacancies at the

Hematite Surface: Pristine Case and with a Chlorine Adatom. *Phys. Chem. Chem. Phys.* **2020**, *22*, 25380–25389.

(17) Pyeon, M.; Ruoko, T. P.; Leduc, J.; Gönüllü, Y.; Deo, M.; Tkachenko, N. V.; Mathur, S. Critical Role and Modification of Surface States in Hematite Films for Enhancing Oxygen Evolution Activity. *J. Mater. Res.* **2018**, *33*, 455–466.

(18) Kim, C. Y. Atomic Structure of Hematite (α-Fe_2O_3) Nanocube Surface; Synchrotron X-Ray Diffraction Study. *Nano-Structures and Nano-Objects* **2020**, *23*, 100497.

(19) Liu, Y.; Smith, R. D. L. Identifying Protons Trapped in Hematite Photoanodes through Structure-Property Analysis. *Chem. Sci.* **2020**, *11*, 1085–1096.

(20) Chernyshova, I. V.; Hochella, M. F.; Madden, A. S. Size-Dependent Structural Transformations of Hematite Nanoparticles. 1. Phase Transition. *Phys. Chem. Chem. Phys.* **2007**, *9*, 1736–1750.

(21) Ling, Y.; Wang, G.; Reddy, J.; Wang, C.; Zhang, J. Z.; Li, Y. The Influence of Oxygen Content on the Thermal Activation of Hematite Nanowires. *Angew. Chemie Int. Ed.* **2012**, *51*, 4074–4079.

(22) Wang, Z.; Mao, X.; Chen, P.; Xiao, M.; Monny, S. A.; Wang, S.; Konarova, M.; Du, A.; Wang, L. Understanding the Roles of Oxygen Vacancies in Hematite-Based Photoelectrochemical Processes. *Angew. Chemie Int. Ed.* **2019**, *58*, 1030–1034.

(23) Yang, Q.; Du, J.; Li, J.; Wu, Y.; Zhou, Y.; Yang, Y.; Yang, D.; He, H. Thermodynamic and Kinetic Influence of Oxygen Vacancies on the Solar Water Oxidation Reaction of α-Fe_2O_3 Photoanodes. *ACS Appl. Mater. Interfaces* **2020**, *12*, 11625–11634.

(24) Zhang, Z.; Karimata, I.; Nagashima, H.; Muto, S.; Ohara, K.; Sugimoto, K.; Tachikawa, T. Interfacial Oxygen Vacancies Yielding Long-Lived Holes in Hematite Mesocrystal-Based Photoanodes. *Nat. Commun.* **2019**, *10*, 4832.

(25) Zhang, X.; Klaver, P.; van Santen, R.; van de Sanden, M. C. M.; Bieberle-Hütter, A. Oxygen Evolution at Hematite Surfaces: The Impact of Structure and Oxygen Vacancies on Lowering the Overpotential. *J. Phys. Chem. C* **2016**, *120*, 18201–18208.

(26) Warschkow, O.; Ellis, D. E.; Hwang, J.; Mansourian-Hadavi, N.; Mason, T. O. Defects and Charge Transport near the Hematite (0001) Surface: An Atomistic Study of Oxygen

Vacancies. *J. Am. Ceram. Soc.* **2002**, *85*, 213–220.

(27) Soares, M. R. S.; Gonçalves, R. H.; Nogueira, I. C.; Bettini, J.; Chiquito, A. J.; Leite, E. R. Understanding the Fundamental Electrical and Photoelectrochemical Behavior of a Hematite Photoanode. *Phys. Chem. Chem. Phys.* **2016**, *18*, 21780–21788.

(28) Wang, L.; Zhu, J.; Liu, X. Oxygen-Vacancy-Dominated Cocatalyst/Hematite Interface for Boosting Solar Water Splitting. *ACS Appl. Mater. Interfaces* **2019**, *11*, 22272–22277.

(29) Liu, Y.; Zhang, J.; Bodappa, N.; Smith, R. D. L. Mechanistic Insights into Lepidocrocite Conversion to Hematite from Variable Temperature Raman Microscopy. *JPhys Energy* **2021**, *3*, 044002.

(30) Zhu, J.; Yang, L.; Wang, H. W.; Zhang, J.; Yang, W.; Hong, X.; Jin, C.; Zhao, Y. Local Structural Distortion and Electrical Transport Properties of $Bi(Ni_{1/2}Ti_{1/2})O_3$ Perovskite under High Pressure. *Sci. Rep.* **2015**, *5*, 18229.

(31) Nguyen, T. H.; Nguyen, T. M. H.; Kang, B.; Cho, B.; Han, M.; Choi, H. J.; Kong, M.; Lee, Y.; Yang, I. S. Raman Spectroscopic Evidence of Impurity-Induced Structural Distortion in SmB6. *J. Raman Spectrosc.* **2019**, *50*, 1661–1671.

(32) Ankudinov, A.; Ravel, B. Real-Space Multiple-Scattering Calculation and Interpretation of x-Ray-Absorption near-Edge Structure. *Phys. Rev. B - Condens. Matter Mater. Phys.* **1998**, *58*, 7565–7576.

(33) Risch, M.; Klingan, K.; Heidkamp, J.; Ehrenberg, D.; Chernev, P.; Zaharieva, I.; Dau, H. Nickel-Oxido Structure of a Water-Oxidizing Catalyst Film. *Chem. Commun.* **2011**, *47*, 11912–11914.

(34) Spray, R. L.; Choi, K. S. Photoactivity of Transparent Nanocrystalline Fe_2O_3 Electrodes Prepared via Anodic Electrodeposition. *Chem. Mater.* **2009**, *21*, 3701–3709.

(35) Gehring, A. U.; Hofmeister, A. M. The Transformation of Lepidocrocite during Heating: A Magnetic and Spectroscopic Study. *Clays Clay Miner.* **1994**, *42*, 409–415.

(36) Glotch, T. D.; Kraft, M. D. Thermal Transformations of Akaganéite and Lepidocrocite to Hematite: Assessment of Possible Precursors to Martian Crystalline Hematite. *Phys. Chem. Miner.* **2008**, *35*, 569–581.

(37) Zandi, O.; Hamann, T. W. Enhanced Water Splitting Efficiency through Selective Surface State Removal. *J. Phys. Chem. Lett.* **2014**, *5*, 1522–1526.

(38) Lin, C. C.; Chiang, M. C.; Chen, Y. W. Temperature Dependence of Fluorine-Doped Tin Oxide Films Produced by Ultrasonic Spray Pyrolysis. *Thin Solid Films* **2009**, *518*, 1241–1244.

(39) Yang, J. K.; Liang, B.; Zhao, M. J.; Gao, Y.; Zhang, F. C.; Zhao, H. L. Reference of Temperature and Time during Tempering Process for Non-Stoichiometric FTO Films. *Sci. Rep.* **2015**, *5*, 15001.

(40) Darab, J. G.; Amonette, A. B.; Burke, D. S. D.; Orr, R. D.; Ponder, S. M.; Schrick, B.; Mallouk, T. E.; Lukens, W. W.; Caulder, D. L.; Shuh, D. K. Removal of Pertechnetate from Simulated Nuclear Waste Streams Using Supported Zerovalent Iron. *Chem. Mater.* **2007**, *19*, 5703–5713.

(41) Canepa, P.; Schofield, E.; Chadwick, A. V.; Alfredsson, M. Comparison of a Calculated and Measured XANES Spectrum of α-Fe_2O_3. *Phys. Chem. Chem. Phys.* **2011**, *13*, 12826–12834.

(42) Calvin, S. *XAFS for Everyone*; CRC Press: Boca Raton, FL, 2013.

(43) Dau, H.; Liebisch, P.; Haumann, M. X-Ray Absorption Spectroscopy to Analyze Nuclear Geometry and Electronic Structure of Biological Metal Centers-Potential and Questions Examined with Special Focus on the Tetra-Nuclear Manganese Complex of Oxygenic Photosynthesis. *Anal. Bioanal. Chem.* **2003**, *376*, 562–583.

(44) Smith, R. D. L.; Pasquini, C.; Loos, S.; Chernev, P.; Klingan, K.; Kubella, P.; Mohammadi, M. R.; Gonzalez-Flores, D.; Dau, H. Spectroscopic Identification of Active Sites for the Oxygen Evolution Reaction on Iron-Cobalt Oxides. *Nat. Commun.* **2017**, *8*, 2022.

(45) Berry, A. J.; O'Neill, H. S. C.; Jayasuriya, K. D.; Campbell, S. J.; Foran, G. J. XANES Calibrations for the Oxidation State of Iron in a Silicate Glass. *Am. Mineral.* **2003**, *88*, 967–977.

(46) Hill, A. H.; Jiao, F.; Bruce, P. G.; Harrison, A.; Kockelmann, W.; Ritter, C. Neutron Diffraction Study of Mesoporous and Bulk Hematite, α-Fe_2O_3. *Chem. Mater.* **2008**, *20*,

4891–4899.

(47) Momma, K.; Izumi, F. VESTA: A Three-Dimensional Visualization System for Electronic and Structural Analysis. *J. Appl. Crystallogr.* **2008**, *41*, 653–658.

(48) Jubb, A. M.; Allen, H. C. Vibrational Spectroscopic Characterization of Hematite, Maghemite, and Magnetite Thin Films Produced by Vapor Deposition. *ACS Appl. Mater. Interfaces* **2010**, *2*, 2804–2812.

(49) Chamritski, I.; Burns, G. Infrared- And Raman-Active Phonons of Magnetite, Maghemite, and Hematite: A Computer Simulation and Spectroscopic Study. *J. Phys. Chem. B* **2005**, *109*, 4965–4968.

(50) Cesar, I.; Sivula, K.; Kay, A.; Zboril, R.; Grätzel, M. Influence of Feature Size, Film Thickness, and Silicon Doping on the Performance of Nanostructured Hematite Photoanodes for Solar Water Splitting. *J. Phys. Chem. C* **2009**, *113*, 772–782.

(51) Mohanty, B.; Wei, Y.; Ghorbani-Asl, M.; Krasheninnikov, A. V.; Rajput, P.; Jena, B. K. Revealing the Defect-Dominated Oxygen Evolution Activity of Hematene. *J. Mater. Chem. A* **2020**, *8*, 6709–6716.

(52) Forster, M.; Potter, R. J.; Ling, Y.; Yang, Y.; Klug, D. R.; Li, Y.; Cowan, A. J. Oxygen Deficient α-Fe_2O_3 Photoelectrodes: A Balance between Enhanced Electrical Properties and Trap-Mediated Losses. *Chem. Sci.* **2015**, *6*, 4009–4016.

(53) Zhao, X.; Feng, J.; Chen, S.; Huang, Y.; Sum, T. C.; Chen, Z. New Insight into the Roles of Oxygen Vacancies in Hematite for Solar Water Splitting. *Phys. Chem. Chem. Phys.* **2017**, *19*, 1074–1082.

(54) Mohamad Noh, M. F.; Ullah, H.; Arzaee, N. A.; Ab Halim, A.; Abdul Rahim, M. A. F.; Mohamed, N. A.; Safaei, J.; Mohd Nasir, S. N. F.; Wang, G.; Mat Teridi, M. A. Rapid Fabrication of Oxygen Defective α-Fe_2O_3(110) for Enhanced Photoelectrochemical Activities. *Dalt. Trans.* **2020**, *49*, 12037–12048.

(55) Shannon, R. D. Revised Effective Ionic Radii and Systematic Studies of Interatomie Distances in Halides and Chaleogenides. *Acta Crystallogr. Sect. A* **1993**, *10*, 751–767.

(56) Gualtieri, A. F.; Venturelli, P. In Situ Study of the Goethite-Hematite Phase Transformation by Real Time Synchrotron Powder Diffraction. *Am. Mineral.* **1999**, *84*,

895–904.

(57) Wolska, E.; Schwertmann, U. Nonstoichiometric Structures during Dehydroxylation of Goethite Emilia. *Cryst. Mater.* **1989**, *189*, 223–237.

(58) Iishi, K. Lattice Dynamics of Corundum. *Phys. Chem. Miner.* **1978**, *3*, 1–10.

(59) Pezzotti, G.; Zhu, W. Resolving Stress Tensor Components in Space from Polarized Raman Spectra: Polycrystalline Alumina. *Phys. Chem. Chem. Phys.* **2015**, *17*, 2608–2627.

Table of Contents: